Tribology International 219 (2026) 111848

Contents lists available at ScienceDirect

Tribology International

journal homepage: www.elsevier.com/locate/triboint

Full Length Article

Enhanced anti-wear properties of HVOF-sprayed Fe-Cr-Mo-C-B high-entropy amorphous composite coatings via heat input modulation

Gaopeng Zou [a,b], Yuxi Qi [a,b], Qianqian Wang [a,b,*], Fangkai Xiong [a,b], Shuaishuai Zhu [c], Feifei Yu [a,b], Huanyu Mo [a,b], Bo Sun [a,b], Mingjuan Cai [d,**], Zhijun Guo [a,b], Qiang Luo [a,b], Zhe Jia [a,b], Baolong Shen [a,b,*]

[a] School of Materials Science and Engineering, Jiangsu Key Laboratory for Advanced Metallic Materials, Southeast University, Nanjing 211189, China
[b] Ministry of Education Key Laboratory of Structure and Thermal Protection for High-Speed Aircraft, Southeast University, Nanjing 211189, China
[c] School of Materials Science and Engineering, Jiangsu Key Laboratory of Advanced Structural Materials and Application Technology, Nanjing Institute of Technology, Nanjing 211167, China
[d] High Magnetic Field Laboratory, Chinese Academy of Sciences, Hefei 230031, China

ARTICLE INFO

Keywords:
High-entropy amorphous composite coating
HVOF
Anti-wear properties
Heat input

ABSTRACT

The wear-resistant applications of amorphous coatings are constrained by their intrinsic brittleness. Herein, we propose that superior wear resistance can be achieved for a novel Fe-Cr-Mo-C-B high-entropy amorphous composite coating by modulating the heat input during the HVOF spraying process. This strategy was demonstrated in coatings produced at high heat input (FR 6.5), which exhibited a remarkably low wear rate of 6.0×10^{-7} $mm^3/(N \cdot m)$, representing a ~ 67 % reduction compared to their counterparts produced at a low heat input (FR 6.2). This enhancement can be attributed to a critical synergistic mechanism: (i) The high heat input promotes the melting and flattening of in-flight powders, resulting in a dense microstructure; (ii) it facilitates the in-situ precipitation of crystalline phase, yielding a synergistic energy dissipation mechanism. The densification of the coating mitigates the initiation and propagation of cracks induced by pores. The presence of hard precipitated phases not only enhances the hardness of the coating but also improves its toughness by the combined effects of the formation of high-density stacking faults, stress-induced disordering, and direct particle shearing, effectively suppressing strain localization and inhibiting premature crack initiation. This work demonstrates that optimizing the dense, multi-phase nanocomposite structure through heat input modulation constitutes an effective anti-wear strategy.

1. Introduction

Demanding service environments, such as those encountered by marine equipment, necessitate materials that possess corrosion and wear resistance simultaneously. Amorphous alloys are well-known for their superior corrosion resistance compared to their crystalline counterparts, primarily due to their long-range disordered atomic topological structure, which lacks conventional crystalline defects such as grain boundaries and dislocations [1–5]. However, this structural advantage does not directly translate into equivalent wear resistance. Exceptional wear resistance requires a synergistic combination of high hardness to minimize abrasive wear by reducing the contact area, along with sufficient ductility to suppress surface microcrack initiation and brittle fracture [6–8]. Unfortunately, despite their ultra-high hardness and near-theoretical strength, amorphous alloys suffer from intrinsic brittleness [9–11]. Under loading, the plastic deformation is highly localized into shear bands, which evolve into cracks and brittle wear particles, thus evoking a micro-cutting mechanism that dramatically accelerates wear [6,12]. This inherent brittleness, coupled with difficulties in bulk forming and the risk of unpredictable failure, severely hinders their widespread engineering application as structural materials.

To address these issues, two primary strategies have been developed. The first strategy focuses on microstructure design, specifically the

* Corresponding authors at: School of Materials Science and Engineering, Jiangsu Key Laboratory for Advanced Metallic Materials, Southeast University, Nanjing 211189, China.
** Corresponding author.
E-mail addresses: qwang678@seu.edu.cn (Q. Wang), mjcai@hmfl.ac.cn (M. Cai), blshen@seu.edu.cn (B. Shen).

https://doi.org/10.1016/j.triboint.2026.111848
Received 28 November 2025; Received in revised form 19 January 2026; Accepted 14 February 2026
Available online 16 February 2026
0301-679X/© 2026 Elsevier Ltd. All rights are reserved, including those for text and data mining, AI training, and similar technologies.

preparation of amorphous alloy matrix composites by introducing ductile or hard secondary crystalline phases [10,13–15]. These crystalline phases enhance overall plasticity and toughness through phase transformations, impede shear band propagation, and promote the formation of multiple shear bands. Wu et al. [10] successfully achieved significant tensile ductility by introducing 25 vol.% B2-structured CuZr crystalline phases into a Zr-based amorphous matrix. These crystalline phases underwent stress-induced martensitic transformation during deformation, resulting in bulk amorphous composites that exhibited both substantial tensile plasticity (~7 %) and high ultimate tensile strength (1650 MPa). Furthermore, Zou et al. [16] introduced a metallic Cu phase into the additively manufactured FeCrMoCB amorphous matrix. The results indicated that the unique amorphous/crystalline microstructure of FeCrMoCB/Cu led to significant reductions in both wear rate and coefficient of friction.

The second strategy involves fabricating amorphous alloys into coatings. This approach effectively decouples the surface functionalities of the material, such as wear resistance, from the macroscopic load-bearing requirements of the substrate, thereby mitigating the risk of catastrophic brittle fracture. To date, the investigations of multiple amorphous alloy systems as surface coating materials, including Fe- [17], Co- [18], Ni- [19], Zr- [20], Cu- [21], Al- [22], and Ti- [23] based amorphous alloys, have been reported. Among them, the $Fe_{48}Cr_{15}Mo_{14}C_{15}B_6Y_2$ (SAM1651) and $Fe_{49.7}Cr_{17.7}Mn_{1.9}Mo_{7.4}W_{1.6}B_{15.2}C_{3.8}Si_{2.4}$ (SAM2X5) amorphous coatings developed by the U.S. Navy, which demonstrate application cases as stable and reliable protection for nuclear waste storage due to excellent corrosion resistance, wear resistance, and radiation resistance [1,24,25]. Subsequently, numerous research groups have been concentrating on compositional modifications, heat treatment, and spraying process analysis based on these two coating systems for the development of new Fe-based amorphous alloy coating. Ye et al. [26] developed a novel $Fe_{34}Ni_{20}Cr_{20}Mo_5B_4C_4P_{12}Nb_1$ ($\Delta S_{mix} = 1.72$ R) high-entropy amorphous coating via high-velocity air fuel spraying technology. The corrosion-wear resistance of the coating is significantly enhanced by minimizing the micro-oxidized zone.

High velocity oxygen fuel (HVOF) spraying technology enables the deposition of dense coatings with retaining a high amorphous fraction by accelerating feedstock powders to supersonic speeds in a high-temperature gas stream [27–29]. Crucially, the process introduces an in-situ heat treatment effect: as particles are successively deposited, the cumulative heat input can induce partial crystallization in the amorphous matrix [30]. This offers a potential pathway to tailor the in-situ precipitation of nanocrystalline phases directly during coating formation. However, a comprehensive understanding of how to precisely modulate this heat input to optimize the trade-off between amorphous retention, functional nanocrystalline precipitation, and coating density for maximum wear resistance remains elusive.

In our previous work [1], we designed a novel $Fe_{31}Cr_{31}Mo_{14}C_{14}B_{10}$ ($\Delta S_{mix} = 1.51$ R) high-entropy amorphous alloy system utilizing data-driven high-throughput methods, which exhibited excellent comprehensive properties, including good corrosion resistance, high hardness, large glass-forming ability (GFA), and exceptional stability. Although the ultimate application targets marine environments, marine components frequently encounter severe mechanical wear. Understanding the intrinsic structure-property relationship under dry sliding conditions is a fundamental prerequisite. Therefore, this study focuses on uncovering how the multi-scale structure, particularly the in-situ precipitates, governs the wear resistance, providing a mechanical basis for future marine applications. Accordingly, this study investigates the fabrication of Fe-Cr-Mo-C-B high-entropy amorphous composite coatings (HEACCs) via HVOF spraying under varying heat inputs. By systematically correlating thermal processing parameters with phase evolution, microstructural features, and tribological performance, we aim to elucidate the synergistic strengthening and toughening mechanisms driven by this tailored multi-scale microstructure.

2. Experiment method

2.1. Sample preparation

$Fe_{31}Cr_{31}Mo_{14}C_{14}B_{10}$ (at.%) powders were synthesized through gas atomization utilizing high-purity argon and industrial-grade raw materials (purity: Fe > 99.5 wt.%, Cr > 99.5 wt.%, Mo > 99.0 wt.%, FeB > 99.0 % and C > 99.9 wt.%). Powders with a particle size of less than 53 μm served as feedstock for the thermal spraying of Fe-Cr-Mo-C-B HEACCs onto 304 stainless steel substrates. The coatings were prepared using a HVOF thermal spray system (HD-8000), with the preparation parameters detailed in Table 1. The heat input during HVOF spraying was regulated by modulating the fuel flow rates to either 6.2 or 6.5 gallons per hour (GPH). Aviation kerosene with a lower heating value (LHV) of approximately 43.5 MJ/kg was used as the fuel. The coating fabricated at a low fuel flow rate of 6.2 GPH was named FR 6.2, and the coating fabricated at a high fuel flow rate of 6.5 GPH was named FR 6.5. Before spraying, the substrate was cleaned with acetone, followed by two thermal sandblasting sessions and one cold sandblasting session. The material employed for sandblasting was 180 mesh white corundum.

2.2. Structure characterization

The compositions of the powders and sprayed coatings were analyzed using an electron probe X-ray micro-analyzer (EPMA, 1720 H), with atomic number-absorption-fluorescence (ZAF) correction. The phase structure of the powders and sprayed coatings was characterized using X-ray diffraction (XRD, D8-Discover) with Cu $K\alpha$ (λ=1.541 Å) radiation and parameters were set as follows: scan speed of 10°/min, scan range from 30° to 60°, voltage of 40 kV, and current of 40 mA. The thermal stability of the powders and coatings was measured using differential scanning calorimetry (DSC, 404F3) at a heating rate of 0.67 K/s. The surface and cross-section morphology of the coatings was observed using field emission scanning electron microscopy (SEM, Navo Nano SEM450), and the elemental distribution was analyzed by energy dispersive spectrometer (EDS). The nanostructure of the coatings, both before and after tribological tests, was further investigated using transmission electron microscopy (TEM, Talos F200X), operating at an acceleration voltage of 200 kV. Element distribution was visualized by a high-angle annular dark field (HAADF) detector and quantified by EDS. The TEM sample of as-sprayed coating was prepared by ion beam milling, while the TEM sample of worn strck subsurface was prepared using the standard focused ion beam (FIB, Helios Nanolab 600i) lift-out method.

2.3. Hardness and tribological tests

Prior to the mechanical and tribological property tests, the samples were ground up to 2000-grit silicon carbide paper and subsequently polished with 0.25 μm diamond paste. The microhardness of the coatings was evaluated using a Vickers micro indenter (FM 700) with loads of 300 gf, 500 gf and 1000 gf, respectively. Nanohardness and Young's modulus were measured using a Nano Indenter G200 system equipped with a diamond Berkovitch tip, which was indented to a maximum load of 50 mN. The tribological properties were investigated using a

Table 1
Spraying parameters employed in the HVOF process.

Parameters	FR 6.2	FR 6.5
Spray distance (mm)	270	270
Oxygen flow rate (SCFH)	1850	1850
Fuel flow rate (GPH)	6.2	6.5
Carrier gas velocity (L/min)	12	12
Powder delivery rate (g/min)	60	60

reciprocating ball-on-block tribometer (Rtec MFT-5000, USA) at room temperature, employing Si_3N_4 balls (diameter: 12.7 mm) as the sliding counterpart. The reciprocating distance was set to 3 mm under a load of 20 N. The sliding speed was maintained at 30 mm/s with a stroke frequency of 5 Hz, and the test duration was 30 min. Wear rates were determined using the volume loss method, where the volume loss was measured with a 3D optical microscope (Bruker Counter GT K 3D). The wear rates were calculated using the following equation:

$$W = \frac{V}{D \times L} \quad (1)$$

Where W is the wear rate in $mm^3/(N{\cdot}m)$, V is the wear loss volume in mm^3, and D is the normal load in N, and L is the sliding distance in m. To ensure statistical reliability, 5 measurements were performed for each hardness test, and 3 parallel experiments were conducted for the tribological tests.

3. Results and discussion

3.1. Microstructure analysis of the powders and coatings

The outer-surface morphology and granulometric distribution of gas-atomized feedstock powders utilized in the HVOF process are illustrated in Fig. 1. As shown in Fig. 1a, the majority of powder particles exhibit a spherical shape with a smooth and dense surface, indicative of favorable fluidity. The average diameter of the feedstock powders is about 36 μm (Fig. 1b). These results indicate that the gas-atomized feedstock powders are suitable for HVOF spraying. The elemental composition of the powders, investigated using EPMA and detailed in Table 2, reveals that the primary constituents of the particles are essentially identical to the nominal composition.

The morphologies of the surface and polished cross-section of HVOF-sprayed coatings are illustrated in Fig. 2. The surfaces of the coatings (Fig. 2a, c) exhibit a dense structure, devoid of significant visible cracking or flaking. The polished cross sections of the FR 6.2 (Fig. 2b) and FR 6.5 (Fig. 2d) coatings, each approximately 400 μm thick, demonstrate strong adhesion to the substrate. The results of the pull-off adhesion tests conducted in accordance with the ASTM C633 standard reveal that both coatings attain an excellent adhesion strength of approximately 90 MPa (see Supplementary Fig. S1). Notably, the FR 6.2 coating exhibits a significant presence of pores, while the FR 6.5 coating reveals a denser structure along with a greater number of bright regions (marked with black circles), which can be associated to crystallized phases. The average porosity of the FR 6.2 and FR 6.5 coatings is quantitatively measured at 3.4 % and 1.0 %, respectively (see Fig. S2).

Fig. 3a presents the DSC curves of the feedstock powders and coatings, all of which exhibit well-defined glass transition temperatures (T_g) and crystallization temperatures (T_x), confirming the presence of the amorphous phase in the samples. The T_g values for the feedstock powders and the FR 6.2, FR 6.5 coatings are 670 °C, 666 °C, and 667 °C, respectively, while the T_x values are 720 °C, 704 °C, and 702 °C, respectively. The T_g and T_x of the coatings are slightly reduced compared to those of the powders. This phenomenon can be attributed to the effects of the HVOF thermal process. Firstly, the introduction of oxygen impurities during spraying may act as heterogeneous nucleation sites, thereby reducing the energy barrier for crystallization. Secondly, the complex thermal history of the coating, which involves particle heating and subsequent heat accumulation from successive passes, may induce structural relaxation or the formation of short-range ordered clusters within the amorphous matrix. Collectively, these factors contribute to reduced thermal stability and the observed shift in characteristic temperatures. Fig. 3b shows the XRD patterns of the Fe-Cr-Mo-C-B powders and coatings. The XRD data of the powders and FR 6.5 are sourced from our previous research [1]. As shown in Fig. 3b, the XRD patterns of both the powders and coatings exhibit a broad hump superimposed with multiple crystalline peaks, further indicating a composite phase structure characterized by both amorphous and crystalline. The amorphous phase content of the powders and coatings is

Table 2
Specific compositions of the coatings and powders.

	Elemental composition (at.%)					
	Fe	Cr	Mo	C	B	O
Powder	29.3	30.6	13.3	16.0	7.5	3.3
FR 6.2	39.9	31.3	13.7	15.6	6.4	3.1
FR 6.5	30.4	30.9	12.7	15.6	6.9	3.5

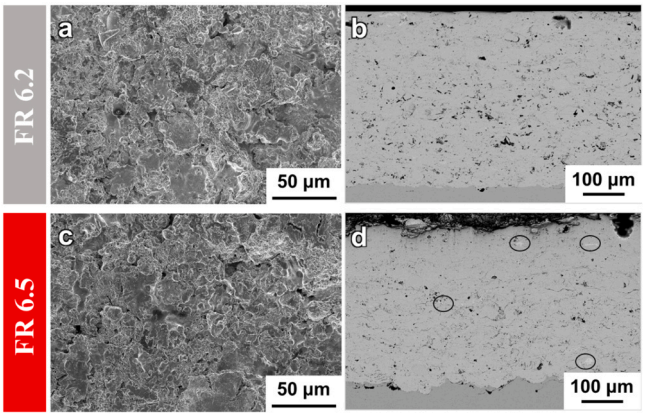

Fig. 2. SEM images of as-sprayed top surface and polished cross-sectional morphology of HVOF-sprayed FR 6.2 (a, b) and FR 6.5 (c, d) coatings.

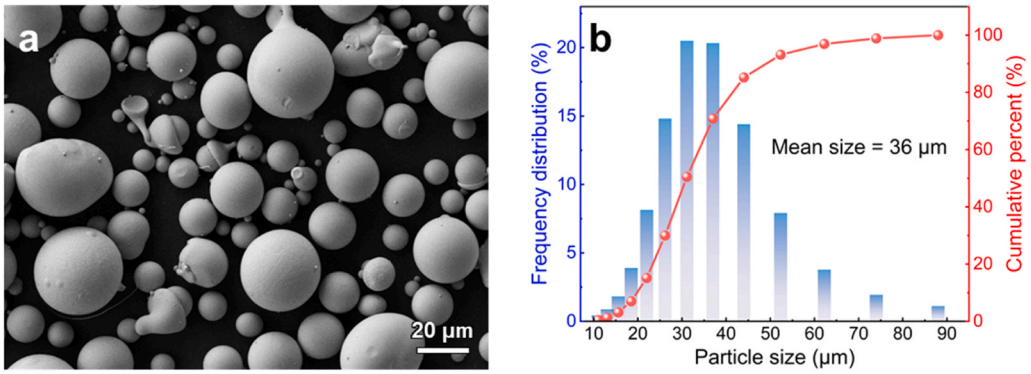

Fig. 1. (a) Surface morphology and (b) size distribution of the gas-atomized $Fe_{31}Cr_{31}Mo_{14}C_{14}B_{10}$ feedstock powders.

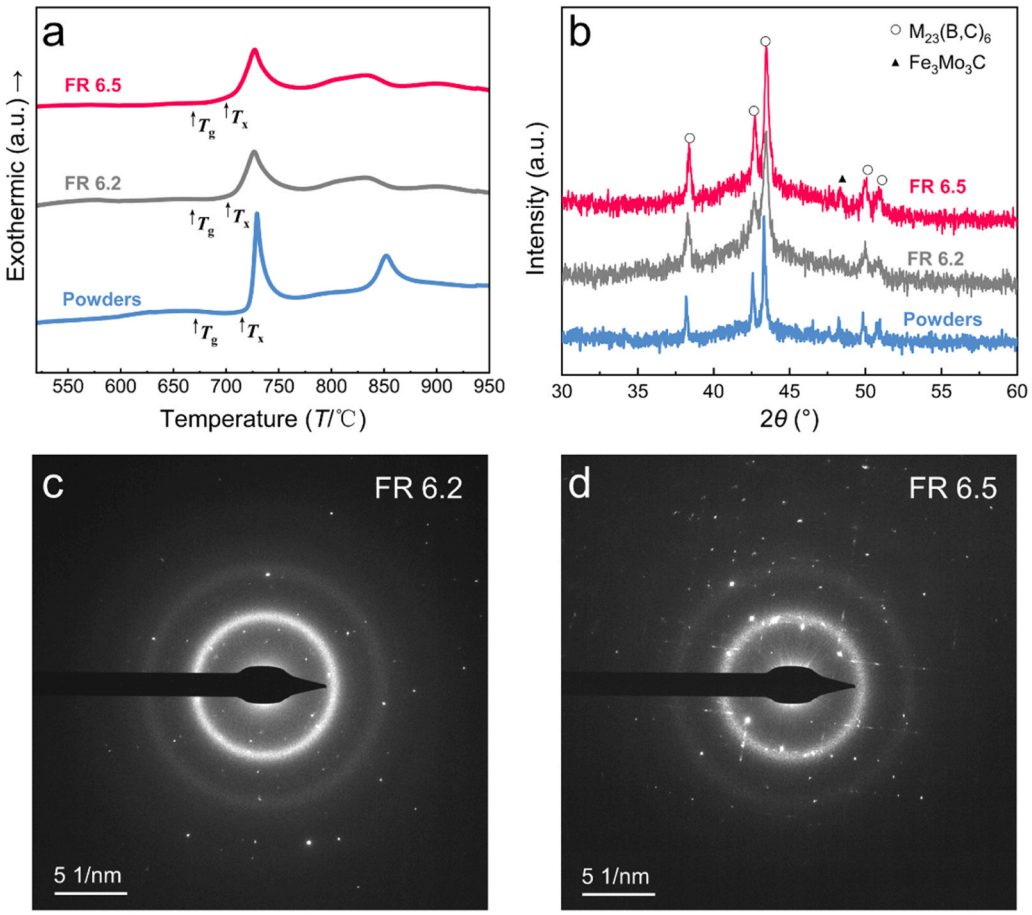

Fig. 3. DSC curves (a) and XRD patterns (b) of the powders, FR 6.2 and FR 6.5 coatings. SAED patterns of the FR 6.2 (c) and FR 6.5 (d) coatings. (Data for powders and FR 6.5 are sourced from Ref. [1]).

estimated based on the area ratio of crystalline peaks to the amorphous hump [28,31]. According to this calculation, the retained amorphous phase fractions in the powders, FR 6.2 coating, and FR 6.5 coating are 69 %, 72 %, and 67 %, respectively. Similar results are obtained from the calculation of crystallization enthalpy derived from DSC curves, yielding values of 68.2 % for FR 6.5, 70.9 % for FR 6.2, and 68.9 % for the powders (see Table S1). The higher retained amorphous phase fraction in the FR 6.2 coating, compared to the powders, can be attributed to the elevated cooling rate associated with the HVOF spraying process. Furthermore, the decrease in the retained amorphous phase fraction in the FR 6.5 coating can be attributed to the higher heat input. The crystalline phases in the FR 6.2 coating can be indexed as $M_{23}(B, C)_6$ (α = 10.591, $Cr_{23}C_6$-type structure, Fm-3m (225)). To be noticed, in addition to the $M_{23}(B, C)_6$ phase, FR 6.5 coating precipitates the Fe_3Mo_3C (cubic, α = 11.135, Fd3m (227)), which is always recognized as a high-temperature phase [32]. The nano-scale microstructural differences between the FR 6.2 and FR 6.5 coatings are further corroborated by the SAED patterns, as illustrated in Fig. 3c and d. The FR 6.2 coating exhibits more pronounced diffuse halo rings, indicating a higher content of the amorphous phase. In contrast, the FR 6.5 coating reveals a more distinct superposition of discrete diffraction spots, thereby confirming the presence of a greater amount of precipitated phase.

To elucidate the nanoscale structure of the FR 6.2 coating, TEM analysis was performed (Fig. 4). The BF-TEM image (Fig. 4a) reveals a multi-phase nanostructure. STEM-EDS elemental mapping confirms the chemical heterogeneity. Three distinct types of precipitates are clearly identified: (i) the bright globular precipitates, which are heavily enriched in Cr and O; (ii) the bright ellipsoidal precipitates, which are enriched in Cr; (iii) the dark ellipsoidal precipitates, which are enriched in both Cr and Mo. The elements B and C are not shown due to the equipment's limitations in detecting these light elements. HRTEM analysis further confirms the structural characteristics of these three phases. Region I, the O-rich inclusion exhibits a disordered nature (Fig. 4b), confirming it is an amorphous oxide. Region II appears largely disordered (Fig. 4c). However, its FFT inset shows faint yet distinct spots superimposed on the amorphous halo, which is a characteristic feature indicative of medium-range order (MRO). The IFFT reconstruction (Fig. 4d), filtered to these spots, clearly visualizes the presence of ordered atomic clusters (nanocrystallites) that could be ascertained as $M_{23}(B, C)_6$ phase through analysis of the *d*-spacing. Most significantly, Region III, the Cr-rich phase is crystalline. Its HRTEM image (Fig. 4e) shows lattice fringes, and the FFT inset presents a regular diffraction pattern. The corresponding IFFT image (Fig. 4f) permits the unambiguous identification of this phase as $M_{23}(C, B)_6$, with lattice spacings measured at d_{620} = 0.167 nm and d_{640} = 0.145 nm. Furthermore, the geometric phase analysis (GPA) map (Fig. 4g) of the region marked by the red square in Fig. 4e reveals severe local strain fields are diffuse and distributed throughout the crystalline precipitate and amorphous matrix.

As illustrated in Fig. 5a, alongside the bright Cr-rich precipitates similar to those found in the FR 6.2 coating, a distinct Mo-rich square precipitate phase is observed in the FR 6.5 coating. Furthermore, this coating exhibits a uniform distribution of the O element, characterized by relatively low signal intensity, indicating a reduced degree of oxidation. HRTEM analysis corroborates the better crystallinity of these precipitates compared to those in the FR 6.2 coating. The Cr-rich precipitate in Region I (Fig. 5b, c) could be identified as a $M_{23}(C, B)_6$-type hard phase (d_{420} = 0.238 nm), while the Mo-rich precipitate in Region II

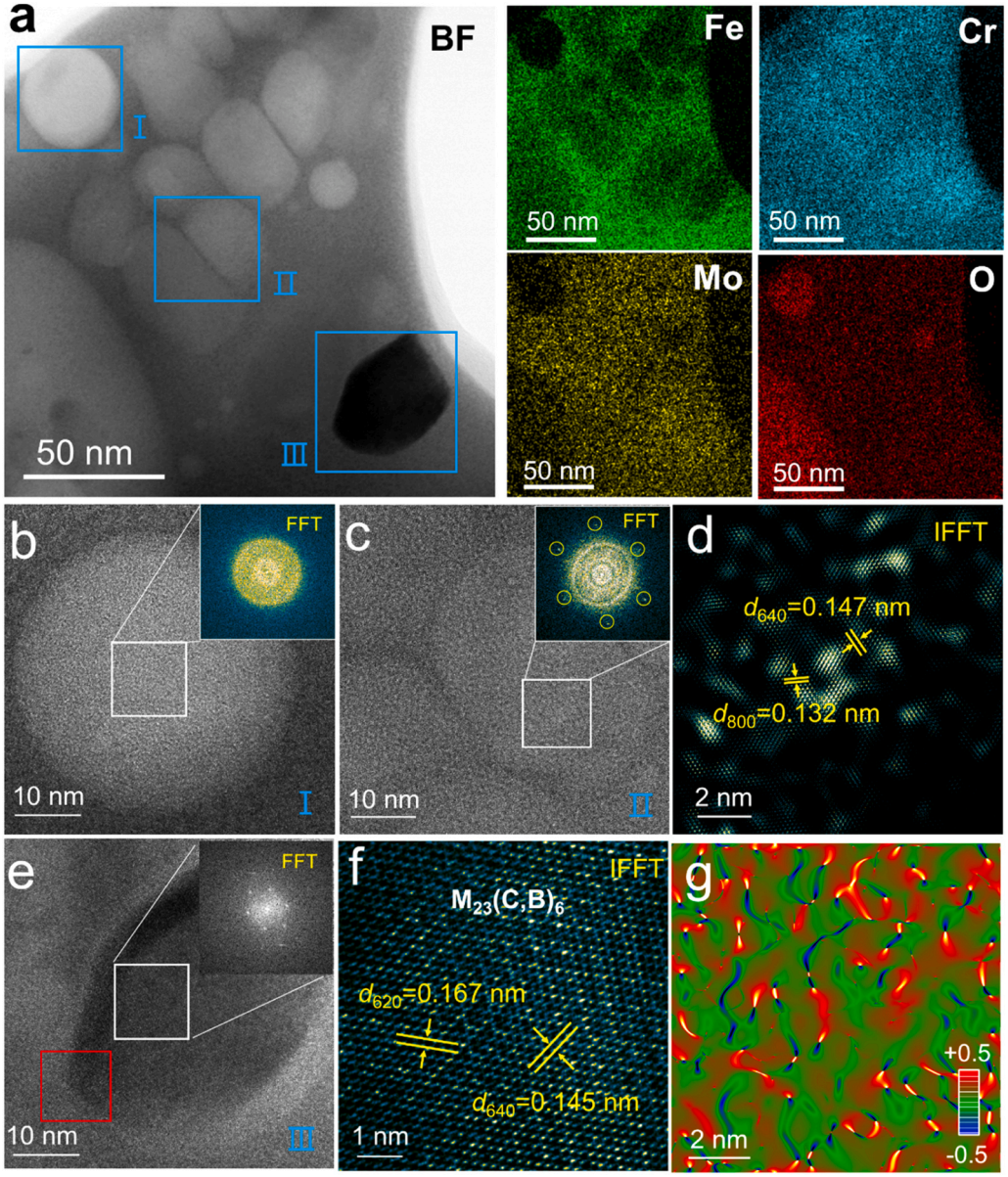

Fig. 4. Nanoscale structural analysis of the FR 6.2 coating. (a) BF-TEM image and corresponding EDS elemental maps for Fe, Cr, Mo, and O. (b) HRTEM image of Region I with its FFT inset. (c) HRTEM image of region II with its FFT inset. (d) IFFT reconstruction of the MRO clusters in Region II. (e) HRTEM image of Region III with its FFT inset. (f) IFFT image of the region marked by white square in (e). (g) GPA map of the region marked red square in (e).

(Fig. 5e, f) could be identified as Fe_3Mo_3C phase (d_{331} = 0.255 nm), consistent with the XRD results. Notably, the GPA maps (Fig. 5d, g) show that the strain fields are no longer diffuse. Instead, intense and localized strain is concentrated directly at the crystalline-amorphous interfaces. This severe interfacial strain, arising from incompatibility during rapid cooling, is the key mechanism governing the distinct tribological behavior of the FR 6.5 coating.

3.2. Nanoindentation and micro-indentation tests

The mechanical properties of as-sprayed coatings were evaluated using nano-indentation and Vickers micro-indentation tests. Nano-hardness and Young's modulus were measured under a constant strain rate, with the typical load-displacement curves illustrated in Fig. 6a. The maximum indentation load was set at 50 mN. As depicted in Fig. 6b, the FR 6.5 coating exhibits higher nanohardness (~16.5 GPa). The ratios of H/E and H^3/E^2, which are often employed to characterize the resistance of materials to plastic deformation and wear, were obtained as summarized in Table 3. The FR 6.5 coating demonstrates higher values of H/E and H^3/E^2, indicating exceptional tribological properties from a purely mechanical perspective [33,34]. Additionally, the results of Vickers microhardness test further confirm the superior hardness (~1024 $HV_{0.3}$) of the FR 6.5 coating (Fig. 6c). The performance of the FR 6.5 coating has been compared with other reported high-performance Fe-based amorphous coatings (Fig. 6d). The FR 6.5 coating, indicated by a red star, is situated in the upper right quadrant, showcasing a remarkable combination of high hardness (~1025 HV) and excellent thermal stability (T_x = 702 °C). Its performance exceeds that of many established Fe-based amorphous coatings [26,28,35–41].

3.3. Tribological behaviors

Fig. 7 shows the tribological properties of FR 6.2 and FR 6.5 coatings at room temperature. The friction coefficient (FC) rises rapidly and reaches a stable stage within 100 s. As depicted in Fig. 7a, the FC of FR 6.5 coating is lower than that of FR 6.2 coating. The wear rates resulting

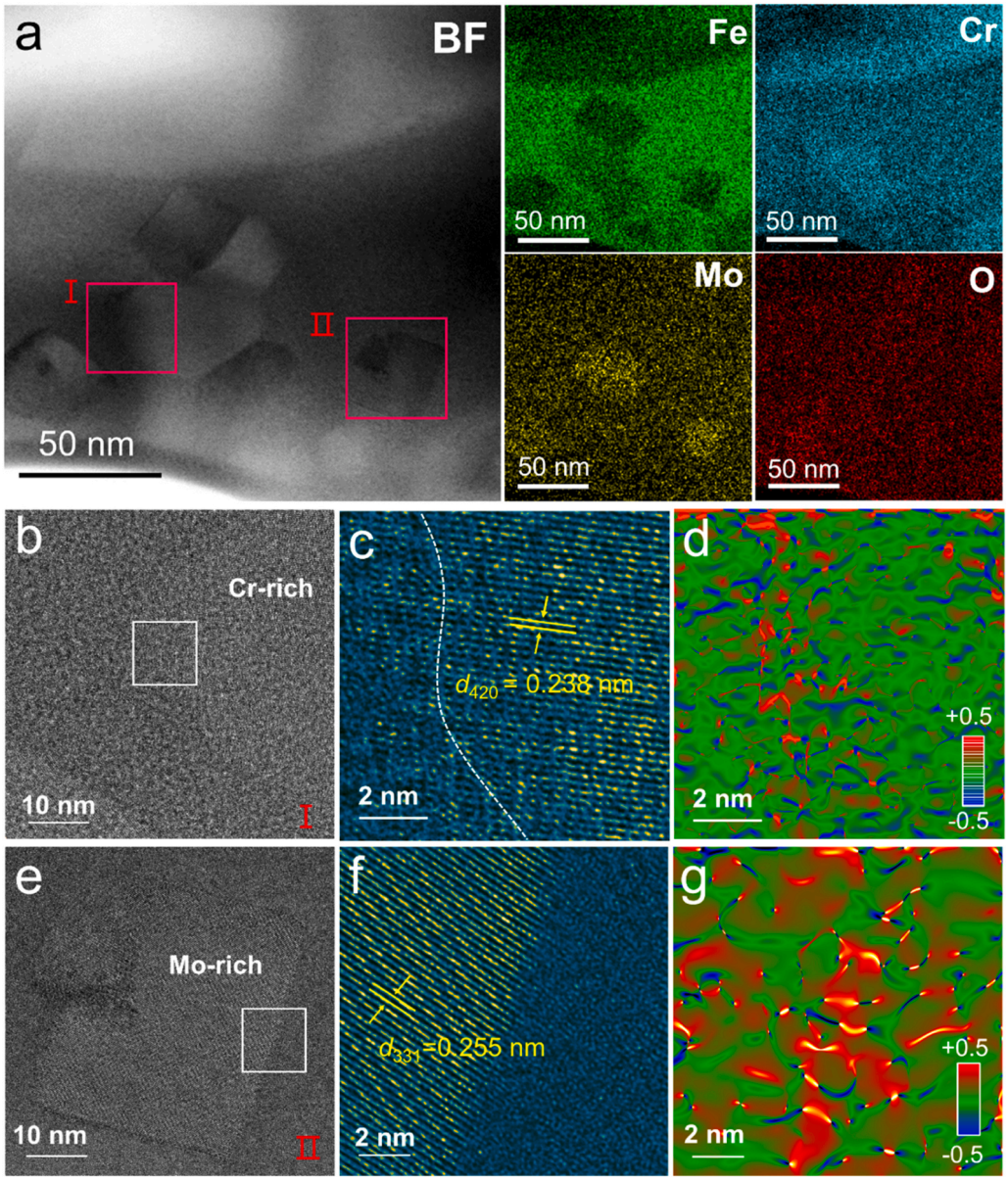

Fig. 5. Nanoscale structural analysis of the FR 6.5 coating. (a) BF-TEM image and corresponding EDS elemental maps for Fe, Cr, Mo, and O. (b) HRTEM image of the precipitate in Region I. Enlarge HRTEM image (c) and GPA map (d) of the region marked by white square in (b). (e) HRTEM image of the precipitate in Region II. Enlarge HRTEM image (f) and GPA map (g) of the region marked by white square in (e).

from sliding are presented in Fig. 7b. The wear rate of FR 6.5 coating is 6.0×10^{-7} $mm^3/(N{\cdot}m)$, which is nearly one-third of that in FR 6.2 coating. Such a wear rate is exceptionally low for metallic alloys subjected to dry sliding wear. The two-dimensional cross-sectional profiles obtained from the wear tracks of FR 6.2 and FR 6.5 coatings are shown in Fig. 7(c, d). Notably, a significantly wider and deeper worn scar was observed on the surface of the FR 6.2 coating compared to that of the FR 6.5 coating. A comparison with the wear rates of other alloys, including Fe-based amorphous coatings, Ni-based alloy coatings, and high-entropy alloy coatings, is shown in Fig. 7e. It is evident that the FR 6.5 coating exhibits superior wear resistance, surpassing most of the reported works [26,28,35,36,42–53].

The morphology and composition of the wear track are revealed through SEM-EDS analyses, as shown in Fig. 8. The wear track of the FR 6.2 coating exhibits a discontinuous tribo-layer (Fig. 8a), whereas the FR 6.5 coating displays a continuous tribo-layer that covers the majority of the wear track (Fig. 8c). EDS analyses indicate that the tribo-layer is rich in O and Si elements (Table 4), implying that material transfer from the grinding balls results in the formation of the friction-induced oxide tribo-layer on the surface. The lower FC of the FR 6.5 coating can be closely related to the presence of a more continuous tribo-layer in the wear track. Furthermore, grooves, cracks, and deep spalling pits can be found at the wear track of FR 6.2 coating (Fig. 8b), revealing both abrasive wear mechanisms and brittle fracture during the sliding process. In contrast, the wear track of FR 6.5 coating exhibits fewer cracks and shallower spalling pits, indicating superior wear resistance (Fig. 8d).

4. Discussion

4.1. Evolution of microstructure induced by heat put

The microstructural evolution of HVOF-sprayed coatings is primarily governed by the particle state upon impact, which is directly influenced by the heat input. The FR 6.5 coating, produced with a higher heat input, imparts greater kinetic and thermal energy to the in-flight particles. This enhanced kinetic energy is the main contributor to the superior density

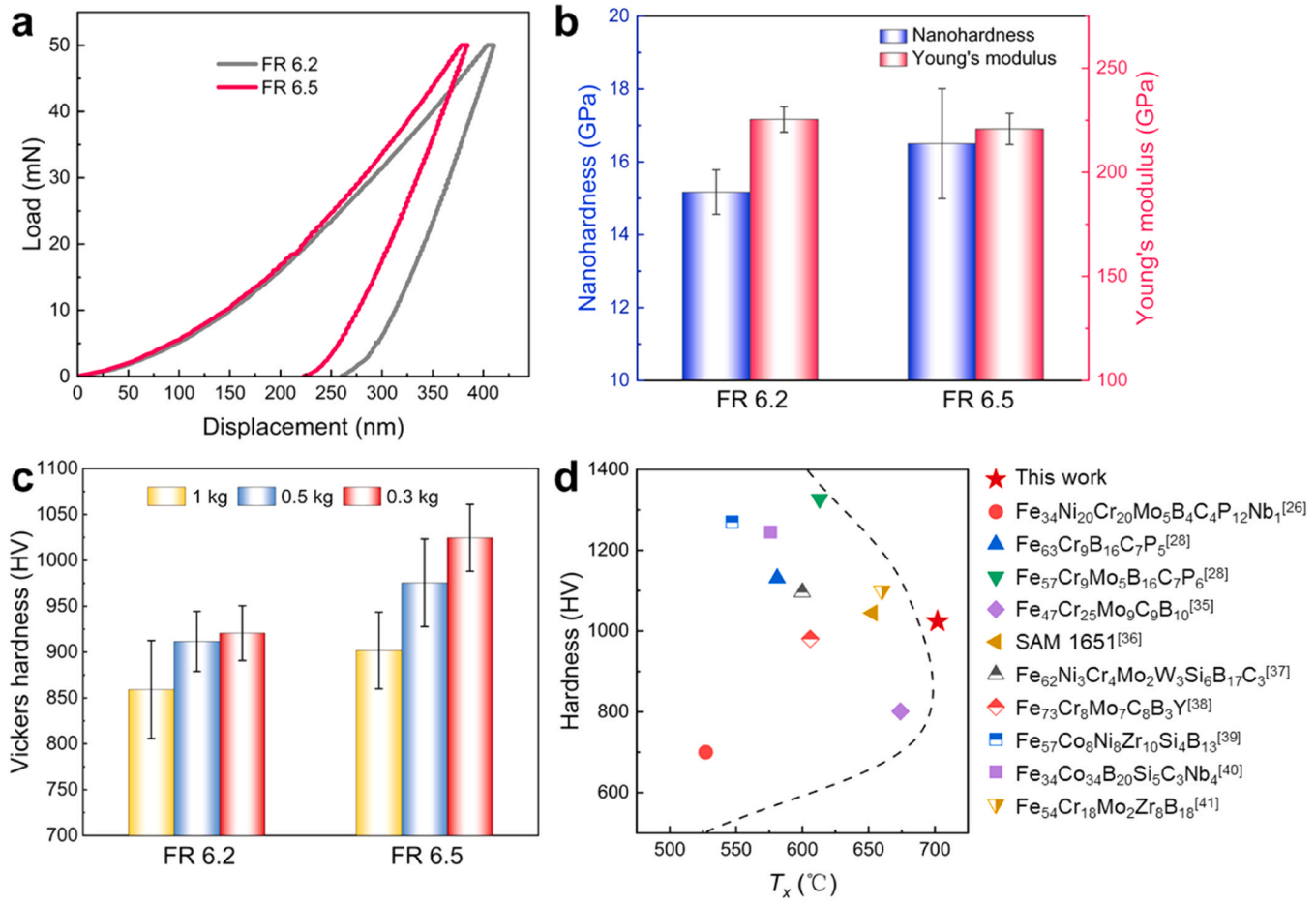

Fig. 6. (a) Typical load-displacement curves for FR 6.2 and FR 6.5 coatings; (b) Measured nanohardness and Young's modulus of FR 6.2 and FR 6.5 coatings; (c) Measured microhardness of FR 6.2 and FR 6.5 coatings under varying loads. (d) Property map comparing the Vickers hardness and T_x of the FR 6.5 coating (This work) with other high-performance Fe-based amorphous coatings from literatures. [26,28,35–41].

Table 3
Summary of mechanical properties of as-sprayed coatings.

Sample	Nanohardness (GPa)	Young's modulus (GPa)	H/E	H^3/E^2 (GPa)	$HV_{1.0}$	$HV_{0.5}$	$HV_{0.3}$
FR 6.2	15.2 ± 0.61	225.4 ± 6.1	0.067	0.069	859 ± 53	912 ± 33	921 ± 30
FR 6.5	16.5 ± 1.51	220.8 ± 7.5	0.075	0.092	902 ± 42	976 ± 47	1024 ± 36

of the coating, facilitating significant plastic deformation and flattening of the splats upon impact with the substrate. Such improved spreading behavior ensures effective filling of inter-lamellar voids, thereby minimizing porosity and resulting in a highly dense microstructure [54]. Moreover, the altered particle state also influences the final chemical and phase composition of the coating. The increased particle velocity (kinetic energy) reduces the in-flight residence time, which limits the extent of in-flight oxidation [21,26]. Concurrently, the higher thermal energy of the particles, along with the retained heat from successive deposition, enhances the in-situ thermal accumulation of the coating. This elevated temperature provides the necessary thermodynamic driving force and atomic mobility to overcome kinetic barriers for crystallization, thereby promoting crystallization and precipitation of Fe_3Mo_3C high-temperature phase [32], as observed in the FR 6.5 sample.

4.2. Origin of enhanced wear resistance

The superior wear resistance of the FR 6.5 coating is a direct consequence of a synergistic optimization of its tribological and mechanical properties. The analysis reveals two key advantages regarding a more favorable tribological interface and superior intrinsic mechanical properties.

The formation of a more extensive and stable tribo-layer reduces the average FC. The mechanism stabilizing the tribo-layer on FR 6.5 will be discussed in depth later. The lower FC, combined with a higher H/E ratio (indicating better toughness), co-determines the subsurface stress state. The von-Mises stress distribution is calculated based on Hamilton's model to provide the relationship between mechanical and tribological behavior [55], as shown in Fig. 9. The parameters were inputted are based on experiment results. The load was set to 20 N, and the friction coefficient was 0.73 for the FR 6.2 and 0.62 for FR 6.5. The elastic modulus, Poisson's ratio, and the diameter of the Si_3N_4 ball were chosen as 320 GPa, 0.26 and 12.7 mm, respectively. The mechanical properties of the polished coating were adopted, which are obtained from nano-indentation test here. The Young's modulus and yield stress were 225.4 GPa and 5.1 GPa for the FR 6.2 coating and 220.8 GPa and 5.5 GPa for the FR 6.5 coating, respectively. The yield stresses are

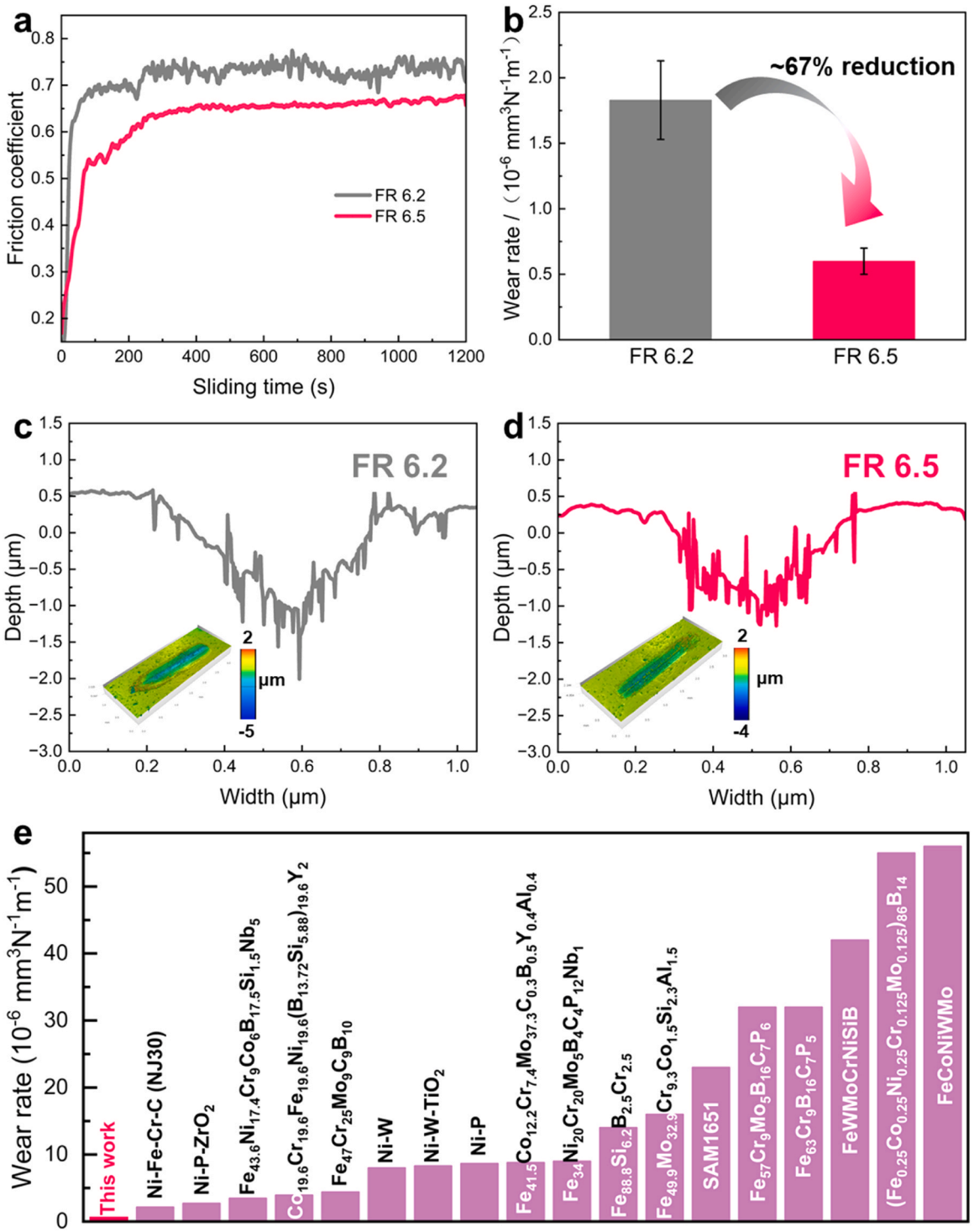

Fig. 7. Tribological properties of FR 6.2 and FR 6.5 coatings at room temperature: (a) Friction coefficient versus sliding time; (b) Wear rate of FR 6.2 and FR 6.5 coatings; (c, d) 2D cross-sectional profiles of the wear tracks; (e) Comparison of different material categories in term of wear rate. Data are from Refs. [26,28,35,36,42–53].

estimated by dividing hardness with 3.0 to convert to a strength value [56]. A Poisson's ratio of 0.3 was used for both coatings. The FR 6.5 coating sustains a significantly lower stress amplitude and a more gradual stress gradient within the critical subsurface region. This mitigated stress state is paramount, as high friction stress is the primary driver for strain localization and delamination [55]. Thus, the FR 6.5 coating fundamentally suppresses these failure modes at the macro-scale.

The enhanced stability of the tribo-layer on FR 6.5 can be attributed to two primary factors. Firstly, the harder FR 6.5 coating (see Fig. 6) provides a rigid foundation for the oxide-based tribo-layer, effectively preventing fractures that could be induced by substrate deformation [57]. Additionally, von Mises stress simulations indicate that the FR 6.5 coating exhibits significantly lower surface stress (see Fig. 9b). This more favorable stress state is insufficient to initiate cracking or delamination, thereby ensuring the continuous integrity of the protective film.

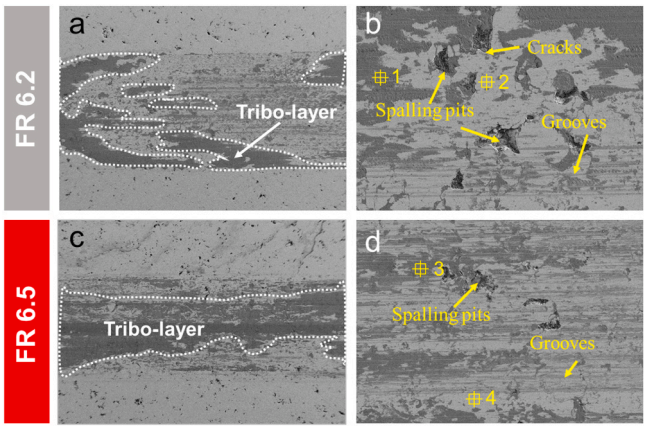

Fig. 8. Surface morphologies of wear tracks: (a, b) SEM images of worn surface of the FR 6.2 coating; (c, d) SEM images of worn tracks of the FR 6.5 coating.

Table 4
Quantitative EDS analysis of wear tracks.

Element (at.%)	Spot 1	Spot 2	Spot 3	Spot 4
O	59.45	6.21	51.99	1.92
C	13.55	32.00	15.01	35.05
Si	4.26	0.20	5.18	0.23
Fe	8.92	24.54	10.84	25.59
Cr	9.56	26.14	11.82	25.99
Mo	4.25	10.90	5.16	11.22

To elucidate the intrinsic toughening mechanism responsible for the superior wear resistance of the FR 6.5 coating, the evolution of the subsurface microstructure after sliding was investigated via TEM. To this end, the FIB method was employed to obtain TEM samples from the worn surface, ensuring that the extraction process was aligned parallel to the sliding direction. It is critical to consider the stability of the reinforcing phase and amorphous matrix under conditions of frictional heating. The local flash temperature at the wear track was calculated using Archard's model [58].

$$T_f = \frac{\mu v (\pi H L)^{1/2}}{8k} \tag{2}$$

where T_f is the local flash temperature, μ is the friction coefficient = 0.62, v is the sliding speed = 0.03 m·s^{-1}, H is the nanoindentation hardness of the coating = 16.5 GPa, L is the normal load = 20 N, and k is the thermal conductivity of coating (k is approximately equal to 7.74 W·m^{-1}·℃$^{-1}$ for Fe-based amorphous alloy [32]). The estimated flash temperature for FR 6.5 is 350 °C, which is insufficient to induce phase decomposition of precipitates and crystallization in the amorphous matrix. No microcracks or oxide layers can be observed in the low-magnification TEM image and corresponding EDS element mapping, indicating the excellent toughness and oxidation resistance of the FR 6.5 coating (Fig. 10a). Notably, the precipitates exhibited complex morphological and microstructural evolution during the sliding process (Fig. 10b). Fig. 10c shows the HRTEM image of the green square region in Fig. 10b. It is evident that high-density stacking faults are generated within the precipitated crystalline phase, as indicated by the streaks in the FFT diffraction patterns shown in the inset of Fig. 10c. Generally, the formation of stacking faults in the ceramic phase is challenging due to the high stacking fault energy [59]. A plausible speculation is that the interface between the amorphous and crystalline phases, characterized by a high local strain field (Fig. 5d and g), serves as a source of partial dislocations. Under the friction stress, these partial dislocations are emitted into the interior of the precipitate phase, resulting in the formation of high-density stacking faults [60]. Furthermore, from the enlarged HRTEM image of the blue square region in Fig. 10c, a localized amorphous structure (area II) can be observed within the precipitates (Fig. 10d), indicating stress-induced structural disordering [61]. Moreover, some of the precipitates are either divided or deformed by the shear band (Fig. 10e, g), and shear steps can also be observed (Fig. 10f, h). These results indicate that the shear band did not merely bypass the hard precipitates but rather cut through them. A similar phenomenon has been reported in other studies [9,62,63]. This observation indicates that there is no interfacial debonding of the hard precipitates; instead, they demonstrate strong interfacial bonding with the matrix due to in-situ precipitation. Consequently, the propagation of shear bands is compelled to sever the hard precipitates, a process that requires substantial energy and thus contributes to improved wear resistance.

The low-porosity structure, which is another essential microstructural origin for the coating, significantly improved wear resistance. Tribologically, pores are inherent micro-defects that are critically detrimental in two ways. As natural stress concentrators, they amplify localized stresses to serve as preferential sites for microcrack initiation. Additionally, pores interact with the tensile stress field of an advancing crack tip, lowering the energy barrier for extension and providing low-

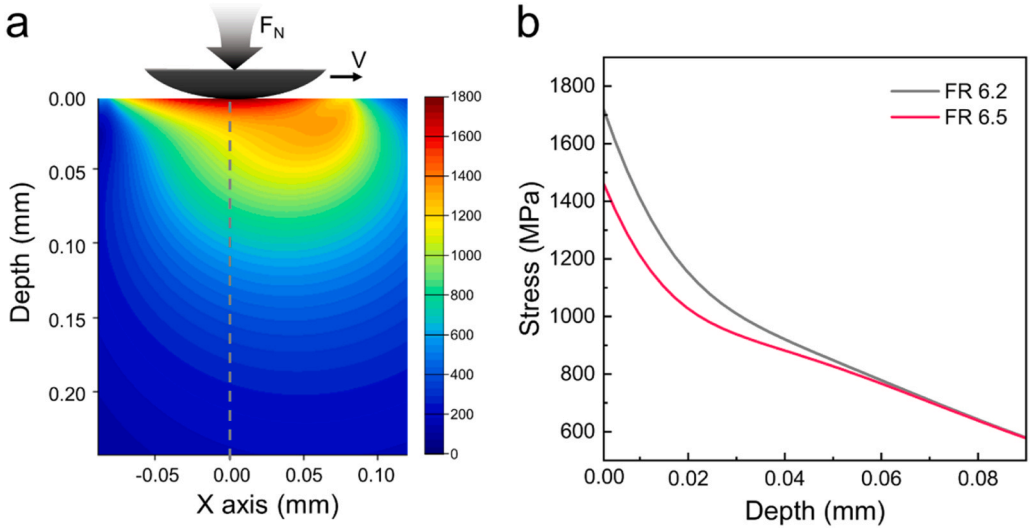

Fig. 9. (a) The von-Mises stress distribution of FR 6.5 coating underneath the sliding contact predicted by Hamilton's model. (b) The variation of stress versus depth along the center of contact (black dashed line in (a)) for FR 6.2 coating and FR 6.5 coating, respectively.

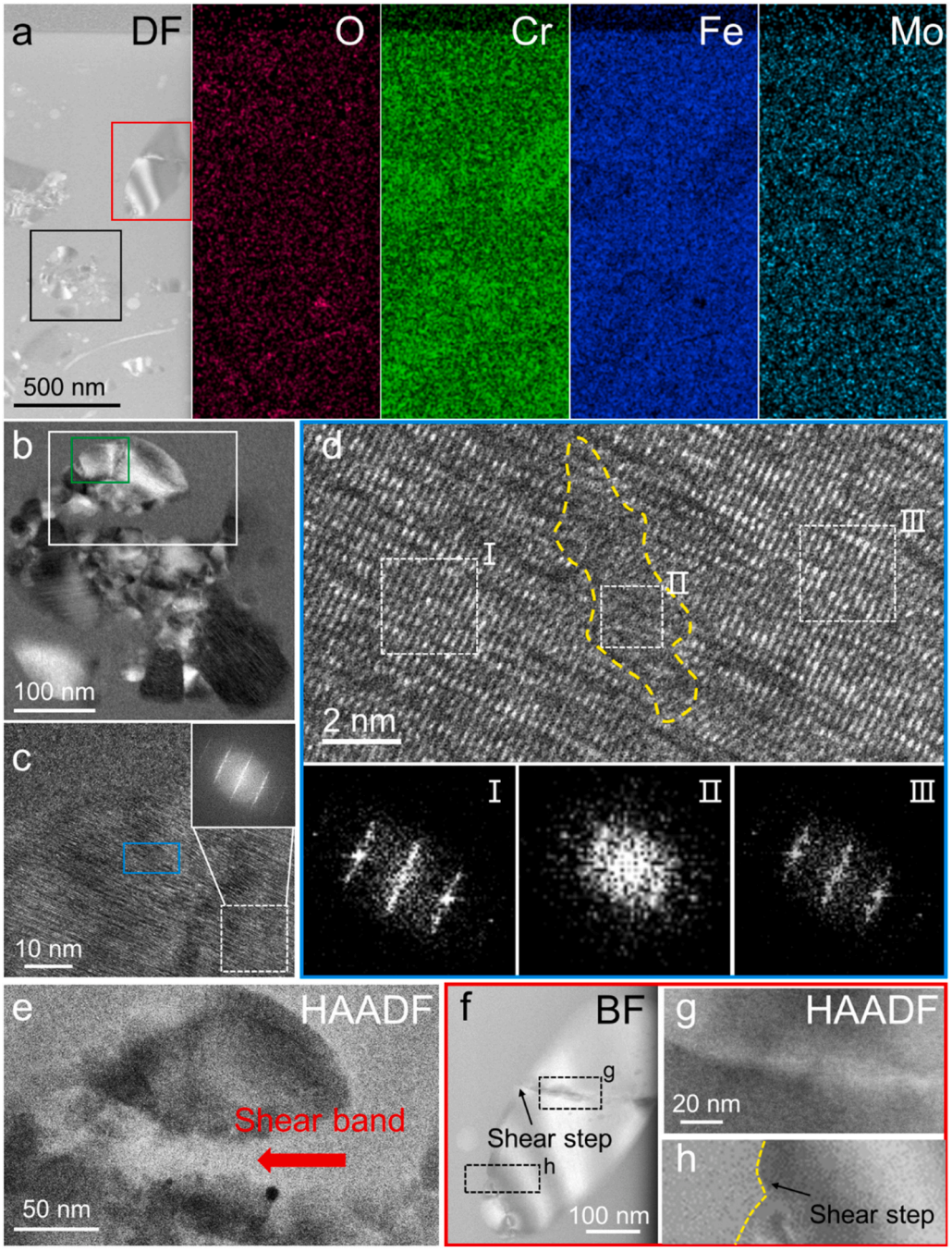

Fig. 10. Cross-sectional TEM characterizations of the FR 6.5 coating after sliding. (a) Dark field TEM image of subsurface microstructure and corresponding EDS elemental distribution. (b) The magnified dark field TEM image of the black square region in (a). (c) HRTEM image of the green square region in (b) and the inset FFT of the white square region. (d) The magnified HRTEM image of the blue square region in (c) and corresponding FFT images of different regions. (e) The HAADF-STEM image of the white square region in (b). (f) Bright field TEM image of the red square region in (a). (g, h) The enlarge images of the black square regions in (f).

resistance pathways for crack propagation and coalescence, which accelerates catastrophic failure. Therefore, the dense, low-porosity structure achieved via high heat input (as discussed in 4.1) is the essential prerequisite. By eliminating pores, which act as stress concentrators and crack initiation sites, the coating's wear behavior is dictated by its advanced intrinsic properties rather than by premature, defect-driven failure.

In summary, the FR 6.5 coating achieves superior wear resistance mainly through the formation of high-density stacking faults, stress-induced disordering, and direct particle shearing, as shown in Fig. 11. Initially, the lattice strain within the $M_{23}(C, B)_6$ and Fe_3Mo_3C precipitates is accommodated by the extensive generation of stacking faults. These planar defects act as an initial energy sink, allowing the hard phases to undergo limited plastic strain without fracture. As the local strain exceeds the capacity of dislocation-mediated plasticity, a stress-induced phase disordering occurs. The crystalline lattice locally collapses into a disordered state. This transformation is a highly efficient energy dissipation mechanism. Ultimately, the primary shear bands originating from the matrix possess sufficient energy to directly shear the precipitates, rather than solely bypassing them. These co-deformation mechanisms suppress crack nucleation, providing the fundamental basis for the coating's exceptional wear resistance.

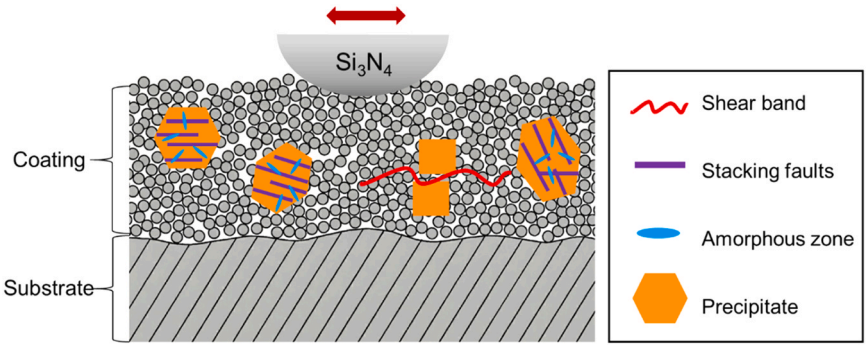

Fig. 11. Schematic representation of the microstructural evolution of the FR 6.5 coating during the friction process.

5. Conclusion

In this study, we demonstrate that modulating heat input is pivotal for optimizing the wear resistance of HVOF-sprayed Fe-Cr-Mo-C-B HEACCs. The high heat input (FR 6.5) coating achieved an exceptional wear rate of 6.0×10^{-7} $mm^3/(N{\cdot}m)$, representing a three-fold improvement over its low-heat-input counterpart. This enhancement is attributed to a critical synergy whereby the high heat input simultaneously eliminates pore defects by creating a dense microstructure and facilitates the in-situ precipitation of a hard ($M_{23}(C, B)_6$ and Fe_3Mo_3C) multi-phase nanocomposite. This nanostructure aids in energy dissipation during the sliding process through the combined effects of the formation of high-density stacking faults, stress-induced disordering, and direct particle shearing, effectively suppressing strain localization and inhibiting premature crack initiation. This work establishes that optimizing the composite nanostructure and coating integrity via modulating heat input is a more effective anti-wear strategy than merely maximizing the amorphous fraction.

CRediT authorship contribution statement

Baolong Shen: Writing – review & editing, Supervision, Funding acquisition. **Zhe Jia:** Methodology. **Mingjuan Cai:** Writing – review & editing, Methodology. **Bo Sun:** Methodology, Formal analysis. **Qiang Luo:** Methodology. **Zhijun Guo:** Methodology, Investigation. **Shuaishuai Zhu:** Methodology. **Fangkai Xiong:** Methodology, Data curation. **Huanyu Mo:** Methodology. **Feifei Yu:** Methodology. **Gaopeng Zou:** Writing – review & editing, Writing – original draft, Methodology, Data curation. **Qianqian Wang:** Writing – review & editing, Supervision, Investigation, Funding acquisition. **Yuxi Qi:** Writing – original draft, Methodology.

Declaration of Competing Interest

The authors declare that they have no known competing financial interests or personal relationships that could have appeared to influence the work reported in this paper.

Acknowledgements

This work was supported by National Natural Science Foundation of China (52571183, 52231005), Jiangsu Provincial Key R&D Program (BE2021088), Open Research Fund of Jiangsu Key Laboratory for Advanced Metallic Materials (AMM2020A01, AMM2024A02, AMM2023B05).

Appendix A. Supporting information

Supplementary data associated with this article can be found in the online version at doi:10.1016/j.triboint.2026.111848.

Data availability

Data will be made available on request.

References

[1] Xiong F, Zou G, Qi Y, Sun B, Zhang B, Zhu S, et al. Data-driven high-throughput screening of Fe-Cr-Mo-C-B amorphous alloy with excellent corrosion and wear resistance. Corros Sci 2026;258:113450. https://doi.org/10.1016/j.corsci.2025.113450.
[2] Li HX, Lu ZC, Wang SL, Wu Y, Lu ZP. Fe-based bulk metallic glasses: glass formation, fabrication, properties and applications. Prog Mater Sci 2019;103:235–318. https://doi.org/10.1016/j.pmatsci.2019.01.003.
[3] Wang DP, Wang SL, Wang JQ. Relationship between amorphous structure and corrosion behaviour in a Zr–Ni metallic glass. Corros Sci 2012;59:88–95. https://doi.org/10.1016/j.corsci.2012.02.017.
[4] Jia Z, Wang Q, Sun L, Wang Q, Zhang L, Wu G, et al. Attractive in situ self-reconstructed hierarchical gradient structure of metallic glass for high efficiency and remarkable stability in catalytic performance. Adv Funct Mater 2019;29. https://doi.org/10.1002/adfm.201807857.
[5] Liang S, Jia Z, Liu Y, Zhang W, Wang W, Lu J, et al. Compelling rejuvenated catalytic performance in metallic glasses. Adv Mater 2018;30:e1802764. https://doi.org/10.1002/adma.201802764.
[6] Liu C, Li Z, Lu W, Bao Y, Xia W, Wu X, et al. Reactive wear protection through strong and deformable oxide nanocomposite surfaces. Nat Commun 2021;12:5518. https://doi.org/10.1038/s41467-021-25778-y.
[7] Lim SC. Recent developments in wear-mechanism maps. Tribol Int 1998;31:87–97. https://doi.org/10.1016/s0301-679x(98)00011-5.
[8] Chen X, Han Z, Li X, Lu K. Lowering coefficient of friction in Cu alloys with stable gradient nanostructures. Sci Adv 2016;2:e1601942. https://doi.org/10.1126/sciadv.1601942.
[9] Wu G, Chan KC, Zhu L, Sun L, Lu J. Dual-phase nanostructuring as a route to high-strength magnesium alloys. Nature 2017;545:80–3. https://doi.org/10.1038/nature21691.
[10] Wu Y, Xiao Y, Chen G, Liu CT, Lu Z. Bulk metallic glass composites with transformation-mediated work-hardening and ductility. Adv Mater 2010;22:2770–3. https://doi.org/10.1002/adma.201000482.
[11] Demetriou MD, Launey ME, Garrett G, Schramm JP, Hofmann DC, Johnson WL, et al. A damage-tolerant glass. Nat Mater 2011;10:123–8. https://doi.org/10.1038/nmat2930.
[12] Greer AL, Rutherford KL, Hutchings IM. Wear resistance of amorphous alloys and related materials. Int Mater Rev 2002;47:87–112. https://doi.org/10.1179/095066001225001067.
[13] Hofmann DC, Suh JY, Wiest A, Duan G, Lind ML, Demetriou MD, et al. Designing metallic glass matrix composites with high toughness and tensile ductility. Nature 2008;451:1085–9. https://doi.org/10.1038/nature06598.
[14] Ma G, Cui H, Du Q, Song X, Zhang H, Zhang H, et al. Gradient structured nanocrystalline–amorphous Fe-based composite coatings with superior strength and wear resistance. J Mater Sci Technol 2026;240:144–55. https://doi.org/10.1016/j.jmst.2025.02.082.
[15] Yan T, Zhang L, Yuan X, Li B, Bai J, Fu H, et al. Simultaneous enhancement of tensile properties and fracture toughness of bulk metallic glass composites. Acta Mater 2025;291:121018. https://doi.org/10.1016/j.actamat.2025.121018.
[16] Zou Y, Qiu Z, Zheng Z, Wang G, Yan X, Yin S, et al. Ex-situ additively manufactured FeCrMoCB/Cu bulk metallic glass composite with well wear resistance. Tribol Int 2021:107112. https://doi.org/10.1016/j.triboint.2021.107112.
[17] Wang Q, Bai X, Sun B, Liu J, Cai Z, Liang X, et al. Influence of Si on tribological behavior of laser cladded Fe-based amorphous/crystalline composite coatings. Surf Coat Technol 2021;405:126570. https://doi.org/10.1016/j.surfcoat.2020.126570.
[18] Tang L, He P, Kang J, Wang L, Ding S, Chen S, et al. Significantly enhanced mechanical and tribological properties of Co-based alloy coatings by annealing treatment. Tribol Int 2020;146:106265. https://doi.org/10.1016/j.triboint.2020.106265.

[19] Li R, Jin Y, Li Z, Zhu Y, Wu M. Effect of the remelting scanning speed on the amorphous forming ability of Ni-based alloy using laser cladding plus a laser remelting process. Surf Coat Technol 2014;259:725–31. https://doi.org/10.1016/j.surfcoat.2014.09.067.

[20] Wu H, Liang L, Zeng H, Lan X, Du J, Zhou C, et al. Microstructure and nanomechanical properties of Zr-based bulk metallic glass composites fabricated by laser rapid prototyping. Mater Sci Eng A 2019;765:138306. https://doi.org/10.1016/j.msea.2019.138306.

[21] Kim J, Kang K, Yoon S, Kumar S, Na H, Lee C. Oxidation and crystallization mechanisms in plasma-sprayed Cu-based bulk metallic glass coatings. Acta Mater 2010;58:952–62. https://doi.org/10.1016/j.actamat.2009.10.011.

[22] Zhang LM, Zhang SD, Ma AL, Hu HX, Zheng YG, Yang BJ, et al. Influence of sealing treatment on the corrosion behavior of HVAF sprayed Al-based amorphous/nanocrystalline coating. Surf Coat Technol 2018;353:263–73. https://doi.org/10.1016/j.surfcoat.2018.08.086.

[23] Lan X, Wu H, Liu Y, Zhang W, Li R, Chen S, et al. Microstructures and tribological properties of laser cladded Ti-based metallic glass composite coatings. Mater Charact 2016;120:82–9. https://doi.org/10.1016/j.matchar.2016.08.026.

[24] Löffler JF. Bulk metallic glasses. Intermetallics 2003;11:529–40. https://doi.org/10.1016/s0966-9795(03)00046-3.

[25] Inoue A. Stabilization of metallic supercooled liquid and bulk amorphous alloys. Acta Mater 2000;48:279–306. https://doi.org/10.1016/s1359-6454(99)00300-6.

[26] Ye Y, Guo Z, Zhou Z, Zhang B, Wang Q, Shen B. Improved corrosion and corrosion-wear properties of Fe-based high-entropy amorphous coatings by modulating heat input of HVAF. Corros Sci 2024;232:112049. https://doi.org/10.1016/j.corsci.2024.112049.

[27] Zheng ZB, Zheng YG, Sun WH, Wang JQ. Erosion–corrosion of HVOF-sprayed Fe-based amorphous metallic coating under impingement by a sand-containing NaCl solution. Corros Sci 2013;76:337–47. https://doi.org/10.1016/j.corsci.2013.07.006.

[28] Nayak SK, Faridi MA, M G, Kumar A, Laha T. Fe-based metallic glass composite coatings by HVOF spraying: Influence of Mo on phase evolution, wear and corrosion resistance. Mater Charact 2022;191:112149. https://doi.org/10.1016/j.matchar.2022.112149.

[29] Meghwal A, Schulz C, Hall C, Vogli E, Berndt CC, Ang ASM. Microstructural, mechanical and high-temperature tribological performance of Fe-based fully amorphous and amorphous/crystalline coatings. Surf Coat Technol 2023;475:130114. https://doi.org/10.1016/j.surfcoat.2023.130114.

[30] Guo W, Wu Y, Zhang J, Hong S, Li G, Ying G, et al. Fabrication and characterization of thermal-sprayed Fe-based amorphous/nanocrystalline composite coatings: an overview. J Therm Spray Technol 2014;23:1157–80. https://doi.org/10.1007/s11666-014-0096-z.

[31] Maurya RS, Sahu A, Laha T. Quantitative phase analysis in $Al_{86}Ni_8Y_6$ bulk glassy alloy synthesized by consolidating mechanically alloyed amorphous powder via spark plasma sintering. Mater Des 2016;93:96–103. https://doi.org/10.1016/j.matdes.2015.12.129.

[32] Yao H, Wang L, Zhou Z, Wang B, Tan Z, He D, et al. Thermal transport property correlated with microstructural evolution of Fe-based amorphous alloy. Acta Mater 2020;200:793–802. https://doi.org/10.1016/j.actamat.2020.09.072.

[33] Yeh CH, Hsu WD, Liu BH, Yang CS, Kuan CY, Chang YC, et al. Low-frequency conductivity of low wear high-entropy alloys. Nat Commun 2024;15:4554. https://doi.org/10.1038/s41467-024-49035-0.

[34] Zhou Q, Jiao Z, Huang Z, Shi Y, Li Y, Yin C, et al. Wear-resistant CrCoNi nanocrystalline film via friction-driven surface segregation. Acta Mater 2024;279:120299. https://doi.org/10.1016/j.actamat.2024.120299.

[35] Cui S, Zhai H, Tong W, Li W, Li X, Fan X, et al. Corrosion and tribo-corrosion behaviors of detonation sprayed Fe-based amorphous coating. Surf Coat Technol 2024;482:130717. https://doi.org/10.1016/j.surfcoat.2024.130717.

[36] Zhang C, Guo RQ, Yang Y, Wu Y, Liu L. Influence of the size of spraying powders on the microstructure and corrosion resistance of Fe-based amorphous coating. Electrochim Acta 2011;56:6380–8. https://doi.org/10.1016/j.electacta.2011.05.020.

[37] Liu G, An Y, Guo Z, Chen J, Hou G, Chen J. Structure and corrosion behavior of iron-based metallic glass coatings prepared by LPPS. Appl Surf Sci 2012;258:5380–6. https://doi.org/10.1016/j.apsusc.2012.02.015.

[38] Wang H, Cheng Y, Wan Y, Jeyaprakash N, Wang Y, Ma K, et al. Influence of scanning speed on microstructure and corrosion resistance of Fe-based amorphous coatings by high-speed laser cladding. Surf Coat Technol 2024;479:130449. https://doi.org/10.1016/j.surfcoat.2024.130449.

[39] Wu X, Hong Y. Fe-based thick amorphous-alloy coating by laser cladding. Surf Coat Technol 2001;141:141–4. https://doi.org/10.1016/s0257-8972(01)01263-4.

[40] Zhu YY, Li ZG, Li RF, Li M, Daze XL, Feng K, et al. Microstructure and property of Fe–Co–B–Si–C–Nb amorphous composite coating fabricated by laser cladding process. Appl Surf Sci 2013;280:50–4. https://doi.org/10.1016/j.apsusc.2013.04.077.

[41] Lu Z, Peng X, Tang Y, Han S, Wu Y, Fu E, et al. Corrosion and irradiation behavior of Fe-based amorphous coating in lead-bismuth eutectic liquids. Sci China Technol Sci 2022;65:440–9. https://doi.org/10.1007/s11431-021-1938-0.

[42] Wang Y, Zhang YZ, Liu YT, Liu X, Liu M, Wang HD, et al. Corrosion wear properties of Fe-based amorphous coatings sprayed by supersonic atmospheric plasma spraying. Surf Coat Technol 2025;496:131678. https://doi.org/10.1016/j.surfcoat.2024.131678.

[43] Chen L, Song H, Guo C, Wang S, Jiang F, Xiao M, et al. Corrosion and wear resistance of ultrasonic vibration-assisted laser cladded Fe-based crystal/amorphous composite coatings. Mater Today Commun 2024;41:110377. https://doi.org/10.1016/j.mtcomm.2024.110377.

[44] Song H, Guo C, Chen L, Jiang F, Xiao M, Wang S, et al. Effect of microstructure of overlapping regions on the wear/corrosion resistance performance of laser cladded Fe-based amorphous composite coatings. J NonCryst Solids 2024;643:123189. https://doi.org/10.1016/j.jnoncrysol.2024.123189.

[45] Zhang C, Liu L, Chan KC, Chen Q, Tang CY. Wear behavior of HVOF-sprayed Fe-based amorphous coatings. Intermetallics 2012;29:80–5. https://doi.org/10.1016/j.intermet.2012.05.004.

[46] Chen B, Zhang G, Zhang Z, Wang Z, Guo C, Song X. Improved wear and corrosion resistance of laser-clad $(Fe_{0.25}Co_{0.25}Ni_{0.25}Cr_{0.125}Mo_{0.125})_{86}B_{14}$ coating through annealing treatment. Surf Coat Technol 2023;473:129973. https://doi.org/10.1016/j.surfcoat.2023.129973.

[47] Si C, Duan B, Zhang Q, Cai J, Wu W. Microstructure, corrosion-resistance, and wear-resistance properties of subsonic flame sprayed amorphous Fe–Mo–Cr–Co coating with extremely high amorphous rate. J Mater Res Technol 2020;9:3292–303. https://doi.org/10.1016/j.jmrt.2020.01.024.

[48] Zhao C, Mao Y, Ning B, Wang N, Xie T, Chen Y, et al. A core-shell structure with amorphous-crystalline to enhance wear resistance in NiW coating. Surf Coat Technol 2025;496:131703. https://doi.org/10.1016/j.surfcoat.2024.131703.

[49] Qi X, Li Y, Cui W, Du J, Zhao Y, Li F. Improving the wear and corrosion properties of laser cladded Ni-based composite coatings via regulating in-situ TiB_2-TiC. Ceram Int 2025;51:9442–54. https://doi.org/10.1016/j.ceramint.2024.12.378.

[50] Tan S, Algül H, Kiliçaslan E, Alp A, Akbulut H, Uysal M. The effect of ultrasonic power on high temperature wear and corrosion resistance for Ni based alloy composite coatings. Colloids Surf A Physicochem Eng Asp 2023;656:130345. https://doi.org/10.1016/j.colsurfa.2022.130345.

[51] He Y, Zhang S, He Y, Song R, Zhang Z, Liu B, et al. Effects of yttrium-stabilized zirconia (different yttrium content) doping on the structure, corrosion resistance and wear resistance of Ni-P electroless coating. Colloids Surf A Physicochem Eng Asp 2022;654:130059. https://doi.org/10.1016/j.colsurfa.2022.130059.

[52] Junshan Z, Liang C, Yuankuo L, Yuhao C, Luqian X, Haoli J, et al. Dry wear and corrosive wear behavior of laser-cladded $Co_{19.6}Cr_{19.6}Fe_{19.6}Ni_{19.6}(B_{13.72}Si_{5.88})_{19.6}Y_2$ and $Fe_{43.6}Ni_{17.4}Cr_9Co_6B_{17.5}Si_{1.5}Nb_5$ coatings. Surf Coat Technol 2024;485:130920. https://doi.org/10.1016/j.surfcoat.2024.130920.

[53] Dehestani M, Sharafi S, Khayati GR. Electrodeposited FeCoNiWMo high entropy alloy/SiC nanocomposite coatings: Microstructure, mechanical properties and corrosion resistance. Intermetallics 2023;162:107988. https://doi.org/10.1016/j.intermet.2023.107988.

[54] Zhang E, Zhang Z, Jing Z, Yuan J, Ma C, Yan S, et al. Research progress on process optimization of thermal-sprayed iron-based amorphous coatings. Integr Mater Manuf Innov 2025;14:247–75. https://doi.org/10.1007/s40192-025-00408-3.

[55] Ren Y, Zhou Q, Hua D, Huang Z, Li Y, Jia Q, et al. Wear-resistant CoCrNi multi-principal element alloy at cryogenic temperature. Sci Bull 2024;69:227–36. https://doi.org/10.1016/j.scib.2023.12.003.

[56] Zhang P, Li SX, Zhang ZF. General relationship between strength and hardness. Mater Sci Eng A 2011;529:62–73. https://doi.org/10.1016/j.msea.2011.08.061.

[57] Leyland A, Matthews A. On the significance of the H/E ratio in wear control: a nanocomposite coating approach to optimised tribological behaviour. Wear 2000;246:1–11. https://doi.org/10.1016/S0043-1648(00)00488-9.

[58] Guo H, Zhang S, Sun W, Wang J. Differences in dry sliding wear behavior between HVAF-sprayed amorphous steel and crystalline stainless steel coatings. J Mater Sci Technol 2019;35:865–74. https://doi.org/10.1016/j.jmst.2018.11.006.

[59] Chen Y, Guo T, Pang X, Qiao L. Formation of high-density stacking faults in ceramic films induced by Ti transition layer. Scr Mater 2022;211:114496. https://doi.org/10.1016/j.scriptamat.2021.114496.

[60] Yang W, Qian L, Luo J, Lu W, Gao Z, Cheung CF, et al. Amorphous phase crystallization-involved cooperative deformation mechanism in a crystalline-amorphous nanostructured compositionally complex alloy. Acta Mater 2026;302:121673. https://doi.org/10.1016/j.actamat.2025.121673.

[61] Du J, Guo S, Feng H, Linghu C, Li W, Wang P, et al. Hyper-range amorphization unlocks superior damage tolerance in alloys. Nat Commun 2025;16:10390. https://doi.org/10.1038/s41467-025-65379-7.

[62] Zhang L, Zhang J, Ke H, Sun B, Zhu Z, Wang Y, et al. On low-temperature strength and tensile ductility of bulk metallic glass composites containing stable or shape memory β-Ti crystals. Acta Mater 2022;222:117444. https://doi.org/10.1016/j.actamat.2021.117444.

[63] Hofmann DC, Suh JY, Wiest A, Duan G, Lind ML, Demetriou MD, et al. Designing metallic glass matrix composites with high toughness and tensile ductility. Nature 2008;451:1085–9. https://doi.org/10.1038/nature06598.